Complex Analysis of Askaryan Radiation: UHE-ν Identification and Reconstruction via the Hilbert Envelope of Observed Signals

Jordan C. Hanson* and Raymond Hartig

Department of Physics and Astronomy, Whittier College

(Dated: October 5, 2025)

The detection of ultra-high energy neutrinos (UHE-ν), with enegies above 10 PeV, has been a long-time goal in astroparticle physics. Autonomous, radio-frequency (RF) UHE-ν detetectors have been deployed in polar regions that rely on the Askaryan effect in ice for the neutrino signal. The Askaryan effect occurs when the excess negative charge within a UHE-ν cascade radiates in a dense medium. UHE-ν can induce cascades that radiate in the RF bandwidth above thermal backgrounds. To identify UHE-ν signals in data from Askaryan-class detectors, analytic models of the Askaryan electromagnetic field have been created and matched to simulations and laboratory measurements. These models describe the Askaryan electromagnetic field, but leave the effects of signal propagation through polar ice and RF channel response to simulations. In this work, a fully analytic Askaryan model that accounts for these effects is presented. First, formulas for the observed voltage trace and its Hilbert envelope are calculated. Second, the analytic model is compared to UHE-ν signals at 100 PeV from NuRadioMC, a key Monte Carlo toolset in the field. Correlation coefficients between the analytic signal envelope and MC data in excess of 0.94 are found, and 99.99% of UHE-ν signals pass a correlation threshold of $\rho = 0.4$. Analysis of RF thermal noise reveals that just 0.2 background events have $\rho \geq 0.4$ in 5 years at a 1 Hz thermal trigger rate. Finally, we present a preliminary reconstruction of the logarithm of the UHE-ν cascade energy from a single string of RF channels.

Keywords: Ultra-high energy neutrino; Askaryan radiation; Mathematical physics

I. INTRODUCTION

Cosmic neutrinos with energies up to 100 PeV have been detected by the IceCube and KM3NeT collaborations [1–8]. Previous analyses indicate that the discovery of UHE-ν flux above 5 PeV requires large Askaryan-class detectors [9]. UHE-ν could reveal the source of ultra-high energy cosmic rays (see sections 3.1-3.3 of [10]). Further, studying electroweak interactions at these energies is impossible on Earth, and Askaryan-class neutrino detectors provide new data (see section 3.4 of [10]).

J. C. Hanson and R. Hartig presented the first fully analytic model of the Askaryan field in the time-domain (HH2022) [11]. The model builds on earlier work from J. C. Hanson and A. L. Connolly (JCH+AC) for spectral filtering due to coherence effects and the form factor of the instantaneous charge distribution (ICD) [12]. When correlated against semi-analytic parameterizations used in NuRadioMC (ARHZ2020), which involve numeric convolution of UHE-ν cascade data with an analytic vector potential, the HH2022 model yields correlation coefficients in excess of 0.95 [11, 13]. This allows precise reconstruction of UHE-ν cascade parameters, but is limited to comparisons between the simulated and theoretical $\vec{E}$-fields.

Askaryan-class detectors actually observe voltage traces that represent the RF detection channel response, convolved with $\vec{E}$-fields that have propagated through kilometers of polar ice. NuRadioMC accounts for these effects by incorporating measurements from years of lab field work [14–25]. In this work, we present the first fully analytic Askaryan model in the time-domain that matches the observed voltage traces. In practice, it is common to compute the Hilbert envelope of voltage traces from RF channels before cross-correlating them. This is done to remove oscillations introduced by the RF antennas in the channels, which can confuse cross-channel timing and reconstruction. Our calculations include both the voltage trace, and the Hilbert envelope of the trace. The work is organized as follows. Units, definitions, and notational conventions are given in Sec. II. In Sec. III, the calculations of the observed voltage trace and Hilbert envelope of the trace are given. These results are compared to NuRadioMC output in Sec. IV. In Sec. VI, the key findings are summarized.

II. UNITS, DEFINITIONS, AND CONVENTIONS

The analysis is based on two analytic functions: the Askaryan signal, $s(t)$, and the RF channel response, $r(t)$. The observed voltage trace in an Askaryan-class detector is $r(t) * s(t)$, the convolution of $r(t)$ and $s(t)$. Let $\hat{s}(t)$ represent the Hilbert transform of $s(t)$, and let $j = \sqrt{-1}$. The *analytic signal* and *signal envelope* are defined by

$$s_a(t) = s(t) + j\hat{s}(t) \tag{1}$$

$$\mathcal{E}_s(t) = |s_a(t)| \tag{2}$$

The signal envelope actually observed by Askaryan-class detectors is the envelope of $r(t) * s(t)$, written as $\mathcal{E}_{r*s}(t)$. The result for $\mathcal{E}_{r*s}(t)$ depends on the model for

————
*Electronic address: jhanson2@whittier.edu

Variable	Definition	Units
c	speed of light in medium	m ns^{-1}
r	distance to cascade peak	m
t_{r}	$t - r/c$	ns
θ_{C}	Cherenkov angle	radians
θ	viewing angle from cascade axis	radians
a	longitudinal cascade length (see [26])	m
n_{max}	max excess cascade particles (see [26])	none
E_0	$\propto n_{\max} a$ (see [26])	V GHz^{-2}
p	$\frac{1}{2}(a/c)^2 (\cos\theta - \cos\theta_C)^2$ (see [11])	ns^2
ω_0	$\sqrt{\frac{2}{3}}(c\sqrt{2\pi}\rho_0)/(\sin\theta)$ (see [12])	GHz
$\sqrt{2\pi}\rho_0$	lateral ICD width (see [12])	m^{-1}

TABLE I: Parameters relevant for Eq. 3.

$s(t)$, taken to be Eq. 28 in HH2022 [11]:

$$r\vec{E}(t_{\mathrm{r}}, \theta) = -\frac{E_0 \omega_0 \sin(\theta)}{8\pi p} t_{\mathrm{r}} e^{-\frac{t_{\mathrm{r}}^2}{4p} + p\omega_0^2} \operatorname{erfc}(\sqrt{p}\omega_0) \quad (3)$$

The parameters of Eq. 3 are shown in Tab. I. Though Ralston and Buniy (RB) [26] used c for the vacuum value of the speed of light, the formulae for $r\vec{E}$ presented in [26] refer to the wavenumber k in the medium, which is proptional to the index of refraction. Thus, the use of c in this work refers to the speed of light in the medium. For example, a phase factor of $\exp(jkr)$ could also be written $\exp(jr\omega/c)$, if c refers to the value in the medium. The distance r is between the observer and the radiating charge at the cascade peak. The longitudinal length over which $\Delta r < \lambda$, the RF wavelength in ice, is named the *coherence zone* Δz_{coh} in the RB model. The Δz_{coh} is limited by what RB call the "acceleration argument," that $r(t)$ is accelerating while keeping $\Delta r < \lambda$.

The time t is the independent variable of the inverse Fourier transform of the equations in [26]. The delayed time is $t_{\mathrm{r}} = t - r/c$. The speed c is equal to the vacuum value, divided by the index of refraction n. For RF in ice, $n = 1.78$ and $\theta_{\mathrm{C}} = 55.8$ degrees. The viewing angle θ is the zenith angle in spherical coordinates, if the cascade axis is the z-axis. The Cherenkov angle is $\cos\theta_{\mathrm{C}} = 1/n$ for relativistic cascades. The longitudinal cascade length, a, is set by the cascade physics. The ratio $\eta = (a/\Delta z_{\mathrm{coh}})^2$ corresponds to the far-field limit as $\eta \to 0$, but $\eta \to 0$ is not a requirement. JCH+AC found that η corresponds to a low-pass filter for the RF spectrum with cutoff frequency ω_{C}: $\eta = \omega/\omega_{\mathrm{C}}$ [12].

The $n_{\max}$ parameter is the maximum excess negative cascade charge, and the overall RF amplitude, E_0, is proptional to $n_{\max}a$ [26]. JCH+AC and HH2022 demonstrated that the cutoff frequency ω_0 is related to the instantaneous charge distribution (ICD) and the cascade form factor [11, 12]. Monte Carlo simulations have shown that the lateral dependence of the ICD is exponentially distributed [12, 27]. JCH+AC derived the ICD form factor, $\widetilde{F}(\omega)$, by modeling the lateral component

of the ICD as an exponential distribution. Finally, the authors of HH2022 have shown that the parameter p is related to σ_t, the Gaussian pulse width of $s(t)$ [11]:

$$\sigma_t = \sqrt{2p} \quad (4)$$

The authors of HH2022 have shown that, because $\cos\theta - \cos\theta_{\mathrm{C}} \approx -\sin\theta_{\mathrm{C}}(\theta - \theta_{\mathrm{C}})$ to first order in $\Delta\theta = (\theta - \theta_{\mathrm{C}})$, $p \propto \Delta\theta^2$ to second order, and

$$a\Delta\theta = \frac{c\sigma_t}{\sin\theta_{\mathrm{C}}} \quad (5)$$

Qualitatively, this notion was identified by RB in Sec. III of [26]. The authors of HH2022 analyzed the relationship between a, the cascade energy E_{C} and the critical energy E_{crit} for electromagnetic and hadronic cascades [11]. Let $E_{\mathrm{C}}/E_{\mathrm{crit}} = \Lambda$. Assuming the Greisen and Gaisser-Hillas parameterizaions for electromagnetic and hadronic cascades, respectively, the following relationships for the a-values from electromagentically dominated and hadronically dominated cascades were found:

$$a_{\mathrm{em}} = c_{\mathrm{em}}\sqrt{\ln\Lambda} \quad (6)$$

$$a_{\mathrm{had}} = c_{\mathrm{had}}\sqrt{\ln\Lambda} \quad (7)$$

The values for c_{em} and c_{had} are calculated in Sec. V. From Eq. 5, the fractional error in $\ln\Lambda$ is:

$$\frac{\sigma_{\ln\Lambda}}{\ln\Lambda} = 2\left(\frac{\sigma_a}{a}\right) \quad (8)$$

Equation 8 corresponds to Eq. 42 in [11], and has been corrected for units. Equations 4-8 imply measurements of a and $\Delta\theta$ yield $\ln\Lambda$, and that the relative error in $\ln\Lambda$ is proportional to the relative error in a.

III. CALCULATION OF THE MAIN RESULTS

The parameters in Eq. 3 that do not depend on time can be folded into a single constant, E_0, leaving only the time-dependence. Let the signal model $s(t)$ be

$$s(t) = -E_0 t e^{-\frac{1}{2}(t/\sigma_t)^2} \quad (9)$$

This is the *off-cone* equation from [11]. The parameter σ_{t} is the pulse width, and it depends two quantities: a and $\Delta\theta$. The parameter E_0 is the amplitude normalization, and the dependencies on other parameters can be determined from Eq. 3 and Tab. I. The Hilbert transform $\widehat{s}(t)$ is equivalent to the convolution of $s(t)$ and the tempered distribution $h(t) = 1/(\pi t)$. The implication in the Fourier domain is that the negative frequencies in the spectrum of $\hat{s}(t)$ vanish, while the positive ones are doubled. Let the $\operatorname{sgn}(f)$ be -1 if $f < 0$, 0 if $f = 0$, and

1 if $f > 1$, and let $S(f)$ be the Fourier transform of $s(t)$. The Fourier transform of the analytic signal $s_{\mathrm{a}}(t)$ is

$$\mathcal{F}\{s_{\mathrm{a}}(t)\}_f = S_{\mathrm{a}}(f) = S(f)(1 + \mathrm{sgn}\, f) \qquad (10)$$

Thus, if $f < 0$, $S_a(f) = 0$, and $S_a(f) = 2S(f)$ if $f \geq 0$. Taking the inverse Fourier transform of Eq. 10, the analytic signal may be written in terms of $S(f)$:

$$s_{\mathrm{a}}(t) = 2 \int_0^\infty S(f) e^{2\pi j f t} df \qquad (11)$$

The Fourier transform of Eq. 9 is

$$S(f) = E_0 \sigma_t^3 (2\pi)^{3/2} j f e^{-2\pi^2 f^2 \sigma_t^2} \qquad (12)$$

Using the gaussian spectral width σ_{f} from [12], and the guassian width of $s(t)$ from [11], it was shown in [11] that the uncertainty principle holds for off-cone signals:

$$\sigma_t \sigma_f \geq \frac{1}{2\pi} \qquad (13)$$

The equality is reached in the limit the far-field parameter limits to zero: $\eta \to 0$. This makes the signal spectrum

$$S(f) = E_0 \sigma_t^3 (2\pi)^{3/2} j f e^{-\frac{1}{2}(f/\sigma_f)^2} \qquad (14)$$

Inserting $S(f)$ into Eq. 11, $s_{\mathrm{a}}(t)$ is

$$s_{\mathrm{a}}(t) = \frac{E_0 \sigma_t^3 (2\pi)^{3/2}}{\pi} \frac{d}{dt} \int_0^\infty e^{-\frac{1}{2}(f/\sigma_f)^2} e^{2\pi j f t} df \qquad (15)$$

Let $k^2/4 = \frac{1}{2}(f/\sigma_f)^2$, and $x = t/(\sqrt{2}\sigma_t)$. Equation 15 can be broken into real and imaginary parts:

$$s_{\mathrm{a}}(t) = \frac{E_0 \sigma_t}{\sqrt{2\pi}} \frac{dI}{dx} \qquad (16)$$

$$\Re\{I\} = \int_0^\infty e^{-k^2/4} \cos(kx) dk \qquad (17)$$

$$\Im\{I\} = \int_0^\infty e^{-k^2/4} \sin(kx) dk \qquad (18)$$

The real part of I is even, so it can be extended to $(-\infty, \infty)$ if it is multiplied by $1/2$. The result is

$$\Re\{I\} = \sqrt{\pi} e^{-x^2} \qquad (19)$$

The imaginary part of I is proportional to the *Dawson function*, $D(x)$ [28]:

$$\Im\{I\} = 2D(x) \qquad (20)$$

The overall analytic signal, $s_a(t)$, is

$$s_a(t) = -E_0 \left(t e^{-\frac{1}{2}(t/\sigma_t)^2} - \frac{2j\sigma_t}{\sqrt{2\pi}} \frac{dD(x)}{dx} \right) \qquad (21)$$

The envelope of the signal, $\mathcal{E}_s(t)$, is the magnitude of Eq. 21. Though $D(x)$ is not evaluated analytically, a high-precision algorithm for computing $D(x)$ was given in [29]. As expected, $|s_a(0)| \neq 0$, since $dD(x)/dx = 1 - 2xD(x)$.

The observed data in Askaryan-class detectors is the convolution of the UHE-ν signal from the ice and the detector response function. To generate *signal templates*, Askaryan radiation signals are calculated for the UHE-ν interaction properties, modified by the frequency-dependent RF attenuation of polar ice, and convolved with the RF channel response [14, 15]. Signal templates are cross-correlated with observed data to identify UHE-ν signals. RF detection channels based on RF dipole antennas, however, have resonance frequencies that introduce oscillations not present in the original signal. The oscillations can introduce timing uncertainties. The problem intensifies when the signal-to-noise ratio (SNR) relative to RF thermal noise decreases.

To reduce uncertainties, the Hilbert envelope of observed data is used in cross-correlations instead of the original signals. Thus, an analytic prediction for the Hilbert envelope of the observed data would an effective signal template. An assumption must be made, however, for the RF channel response. The RLC damped oscillator is a suitable circuit model for the RF dipole antennas used in RICE, RNO-G, and the proposed IceCube Gen2 [10, 30]. In fact, an RLC response was first used by RICE at the South Pole a decade ago [31].

There are two paths to calculating the final result, $\mathcal{E}_{r*s}(t)$. The first involves three steps. First, the detector response, $r(t)$ is convolved with $s(t)$. Second, the analytic signal of the result is found. Third, the magnitude of the analytic signal is computed, which can be compared to envelopes of observed signals. The second path involves computing $\mathcal{E}_{r*s}(t)$ directly from $s_a(t)$ and $r_a(t)$. The second option is more straightforward, once a special theorem relating $r_a(t)$, $s_a(t)$, and $\mathcal{E}_{r*s}(t)$ is established. $\mathcal{E}_{s*r}(t)$, $s_a(t)$, and $r_a(t)$ are related by

$$\mathcal{E}_{s*r}(t) = \frac{1}{2}|s_a(t) * r_a(t)| \qquad (22)$$

The proof of Eq. 22 is based on two ideas. First, the Hilbert transform of a function $s(t)$ is equivalent to convolving it with the "tempered distribution" $h(t) = 1/(\pi t)$. Second, computing the Hilbert transform twice yields the original function, multiplied by -1: $h * h * s = -s$. Given the definitions of the analytic signal and the Hilbert transform,

$$(s * r)_a(t) = s * r + j\, \widehat{s * r} \qquad (23)$$

$$\mathcal{E}_{s*r}(t) = |s * r + js * r * h| \qquad (24)$$

However,

$$r_a * s_a = (r + j\hat{r}) * (s + j\hat{s}) \qquad (25)$$

$$r_a * s_a = r * s + jr * \hat{s} + j\hat{r} * s - \hat{r} * \hat{s} \qquad (26)$$

$$r_a * s_a = r * s - r * h * s * h + 2jh * r * s \qquad (27)$$

$$r_a * s_a = r * s - h * h * r * s + 2jh * r * s \qquad (28)$$

$$r_a * s_a = 2r * s + 2jh * r * s \qquad (29)$$

Multiplying both sides $1/2$ and taking the magnitude

completes the proof:

$$\frac{1}{2}|r_a * s_a| = |r * s + jh * r * s| = \mathcal{E}_{s*r}(t) \quad (30)$$

Assume that a signal arrives in an RLC damped oscillator at $t = 0$. For $t \geq 0$, the impulse response and corresponding analytic signal are

$$r(t) = R_0 e^{-2\pi\gamma t}\cos(2\pi f_0 t) \quad (31)$$

$$r_a(t) = R_0 e^{-2\pi\gamma t}e^{2\pi j f_0 t} \quad (32)$$

The parameters γ and f_0 are the decay constant and the resonance frequency. Note that the envelope of $r(t)$, $|r_a(t)|$, is $R_0 \exp(-2\pi\gamma t)$, as expected. To prove Eq. 32, first compute the Fourier transform of $r(t)$:

$$R(f) = \frac{R_0}{4\pi j}\left(\frac{1}{f - z_+} + \frac{1}{1 - z_-}\right) \quad (33)$$

$$z_+ = f_0 + j\gamma \quad (34)$$

$$z_- = -f_0 + j\gamma \quad (35)$$

Given Eq. 11, the procedure to find $r_a(t)$ is to multiply the *negative* frequency component at z_- by 0 and the *positive* frequency component at z_+ by 2, and take the inverse Fourier transform. The inverse Fourier transform may be completed by applying Jordan's lemma in the complex plane frequency plane. The residue from the pole at z_+ yields the result.

The goal is now to apply Eq. 22 by convolving $s_a(t)$ with $r_a(t)$. The calculation may be split into two parts: $r_a(t) * \Re\{s_a(t)\}$, and $r_a(t) * \Im\{s_a(t)\}$. Let $u(t)$ represent the Heaviside step function. Starting with $r_a(t) * \Re\{s_a(t)\}$:

$$r_a(t) * \Re\{s_a(t)\} =$$
$$R_0 e^{2\pi j f_0 t}e^{-2\pi\gamma t}u(t) * \left(-E_0 t e^{-\frac{1}{2}(t/\sigma_t)^2}\right) \quad (36)$$

Let $x = t/(\sqrt{2}\sigma_t)$, $y = \tau/(\sqrt{2}\sigma_t)$, and $z = (2\pi j f_0 - 2\pi\gamma)\sqrt{2}\sigma_t$. Changing variables while accounting for the relationship between $u(t)$, x, and y, gives

$$r_a(t) * \Re\{s_a(t)\} =$$
$$-2R_0 E_0\sigma_t^2\int_{-\infty}^{x}e^{z(x-y)}ye^{-y^2}dy \quad (37)$$

Note that the units for the convolution of $r(t)$ and $s(t)$ are $R_0 E_0 \sigma_t^2$. Let $u = x - y$, so that $du = -dy$. The result is

$$r_a(t) * \Re\{s_a(t)\} = 2R_0 E_0\sigma_t^2\left(\frac{dI(x, z)}{dz} - xI(x, z)\right) \quad (38)$$

where

$$I(x, z) = \int_0^{\infty}e^{zu}e^{-(u-x)^2}du \quad (39)$$

Let $b = x + \frac{1}{2}z$. Completing the square in the exponent and substituting $k = u - b$ gives

$$I(x, z) = e^{-x^2}e^{b^2}\int_{-b}^{\infty}e^{-k^2}dk$$
$$= \frac{\sqrt{\pi}}{2}e^{-x^2}e^{b^2}\operatorname{erfc}(-b) \quad (40)$$

Let $b = jq$, and $w(q)$ be the *Faddeeva function* [28]. The integral becomes

$$I(x, z) = \frac{\sqrt{\pi}}{2}e^{-x^2}w(q) \quad (41)$$

The chain rule is required to find dI/dz:

$$\frac{dI}{dz} = \frac{dI}{dq}\frac{dq}{dz} = -\left(\frac{j}{2}\right)\frac{dI}{dq} \quad (42)$$

The final result is

$$r_a(t) * \Re\{s_a(t)\} =$$
$$-\sqrt{\pi}R_0 E_0\sigma_t^2\left(xe^{-x^2}w(q) + \left(\frac{j}{2}\right)e^{-x^2}\frac{dw(q)}{dq}\right) \quad (43)$$

Turning to the convolution of $r_a(t)$ with $\Im(s_a)$,

$$r_a(t) * \Im\{s_a(t)\} =$$
$$\left(R_0 e^{2\pi j f_0 t}e^{-2\pi\gamma t}u(t)\right) * \left(\frac{2E_0\sigma_t^2}{\sqrt{\pi}}\frac{dD(t/\sqrt{2}\sigma_t)}{dt}\right) \quad (44)$$

Note that $f'(t) * g(t) = f(t) * g'(t) = (f(t) * g(t))'$. Thus,

$$r_a(t) * \Im\{s_a(t)\} =$$
$$\frac{2}{\sqrt{\pi}}R_0 E_0\sigma_t^2\frac{d}{dt}\left(e^{2\pi j f_0 t}e^{-2\pi\gamma t}u(t) * D(t/\sqrt{2}\sigma_t)\right) \quad (45)$$

The convolution becomes

$$r_a(t) * \Im\{s_a(t)\} =$$
$$\frac{2}{\sqrt{\pi}}R_0 E_0\sigma_t^2\frac{d}{dt}\int_{-\infty}^{t}e^{(2\pi j f_0 - 2\pi\gamma)(t-\tau)}D(\tau/\sqrt{2}\sigma_t)d\tau \quad (46)$$

Adopting the earlier definitions of x, y, and z gives

$$r_a(t) * \Im\{s_a(t)\} =$$
$$\frac{2}{\sqrt{\pi}}R_0 E_0\sigma_t^2\frac{d}{dx}\int_{-\infty}^{x}e^{z(x-y)}D(y)dy \quad (47)$$

Using Leibniz rule for the fundamental theorem of calculus, and the limiting cases of $D(x)$,

$$r_a(t) * \Im\{s_a(t)\} =$$
$$\frac{2}{\sqrt{\pi}}R_0 E_0\sigma_t^2\left(D(x) + z\int_{-\infty}^{x}e^{z(x-y)}D(y)dy\right) \quad (48)$$

Let $u = x - y$, $z = -k$, and note that $D(x)$ is an odd function. These substitutions give

$$r_a(t) * \Im\{s_a(t)\} =$$
$$\frac{2}{\sqrt{\pi}} R_0 E_0 \sigma_t^2 \left(D(x) + k \int_0^\infty e^{-ku} D(u-x) du \right) \quad (49)$$

The remaining integral is the Laplace transform of the shifted Dawson function, $\mathcal{L}\{D(u-x)\}_k$. The final result is

$$r_a(t) * \Im\{s_a(t)\} =$$
$$\frac{2}{\sqrt{\pi}} R_0 E_0 \sigma_t^2 \left(D(x) + k\mathcal{L}\{D(u-x)\}_k \right) \quad (50)$$

Though a closed analytic form for $\mathcal{L}\{D(u-x)\}_k$ is elusive, evaluating $\mathcal{L}\{D(u-x)\}_k$ numerically is fast and precise.

Combining Eq. 43 and Eq. 50 gives $r_a(t) * s_a(t)$:

$$r_a(t) * s_a(t) =$$
$$- \sqrt{\pi} R_0 E_0 \sigma_t^2 \left(x e^{-x^2} w(q) + \left(\frac{j}{2} \right) e^{-x^2} \frac{dw(q)}{dq} \right) +$$
$$\frac{2j}{\sqrt{\pi}} R_0 E_0 \sigma_t^2 \left(D(x) + k\mathcal{L}\{D(u-x)\}_k \right) \quad (51)$$

The units of convolution should be $R_0 E_0 \sigma_t^2$, and each term in Eq. 51 has these units. Remember that the relationship between q and x is given by

$$q = -jb = -j\left(x + \frac{z}{2} \right) \quad (52)$$

Taking the magnitude of Eq. 51, and multiplying by $1/2$, yields the **Hilbert envelope of the convolution of $s(t)$ with $r(t)$:**

$$\mathcal{E}_{r*s}(t) = \frac{1}{2} |r_a(t) * s_a(t)| \quad (53)$$

To model the full time-dependent voltage trace from detection channels, and not merely the envelope, $s(t) * r(t)$ is required. The calculation may be done analytically, starting with the definition of convolution:

$$s(t) * r(t) = \int_{-\infty}^\infty s(t-\tau) r(\tau) d\tau \quad (54)$$

As in the calculation of $\mathcal{E}_{r*s}(t)$, the Heaviside step function, $u(t)$ is included to ensure causality. Inserting the definitions of $s(t)$, $r(t)$, and $u(t)$ gives

$$s * r =$$
$$-E_0 R_0 \int_{-\infty}^\infty (t-\tau) e^{-\frac{1}{2}\left(\frac{t-\tau}{\sigma_t} \right)^2} \Re\{ e^{2\pi j f_0 \tau} e^{-2\pi\gamma\tau} \} u(\tau) d\tau$$
$$(55)$$

Using the previous definitions of x, y, and z gives

$$s * r = -2 R_0 E_0 \sigma_t^2 \int_0^\infty (x-y) e^{-(x-y)^2} \Re\{ e^{zy} \} dy \quad (56)$$

Note that the $\Re\{\}$ operator can encompass the whole integral, since $s(t)$ is real. Splitting the integral and employing differentiation under the equals sign yields

$$s * r =$$
$$-2 R_0 E_0 \sigma_t^2 \Re \left\{ x e^{-x^2} I(x,z) - \frac{1}{2} e^{-x^2} \frac{dI(x,z)}{dx} \right\} \quad (57)$$

with

$$I(x,z) = \int_0^\infty e^{-y^2+(2x+z)y} dy \quad (58)$$

Let $b = x + \frac{1}{2}z$, and $b = jq$. The calculation resembles that of $r_a(t) * \Re\{s_a(t)\}$. The result for $I(x,z)$ is

$$I(x,z) = \frac{\sqrt{\pi}}{2} w(q) \quad (59)$$

Inserting this result into Eq. 57, gives

$$s * r = -\sqrt{\pi} R_0 E_0 \sigma_t^2$$
$$\Re \left\{ x e^{-x^2} w(q) - \frac{1}{2} e^{-x^2} \frac{dw(q)}{dx} \right\} \quad (60)$$

From the definition of q and the chain rule, $dw(q)/dx = -jdw(q)/dq$, and $dw(q)/dq = -2qw(q) + 2j/\sqrt{\pi}$ [28]. The final result is left in terms of $\Re\{w(q)\}$ and $\Re\{-jdw(q)/dq\}$, which are proportional to the *Voigt functions* [11, 28].

$$s * r = -\sqrt{\pi} R_0 E_0 \sigma_t^2$$
$$\left(x e^{-x^2} \Re\{w(q)\} - \frac{1}{2} e^{-x^2} \Re\left\{ -j\frac{dw(q)}{dq} \right\} \right) \quad (61)$$

To illustrate the accuracy of the model, the *numerically-computed envelope* of Eq. 61 is compared to Eqs. 51-53 in Fig. 1. The *numerical convolution* of $s(t)$ and $r(t)$ is compared to Eq. 61 in Fig. 2.

IV. COMPARISON BETWEEN ANALYTIC CALCULATIONS AND NURADIOMC

NuRadioMC was used to generate UHE-ν interactions in a cylindrical ice volume (see Tab. II). The 100 PeV interactions included charged and neutral electroweak currents, and the LPM effect. The Askaryan model used in NuRadioMC was ARZ2020 [13]. ARZ2020 is a *semi-analytic* parameterization of the Askaryan effect, in which a vector potential $\vec{A}(\vec{r}, t)$ is convolved with the profile of the net charge in the UHE-ν cascade. ARZ2020 accounts for sub-cascades and the LPM effect, and it has been validated against MC simulations [27, 32]. The Askaryan signal model used in NuRadioMC for this analysis was *not* HH2022 [11]. Thus, the correlation between MC output (ARZ2020) and Eqs. 51-53 (HH2022 and this work) is solely on physical grounds.
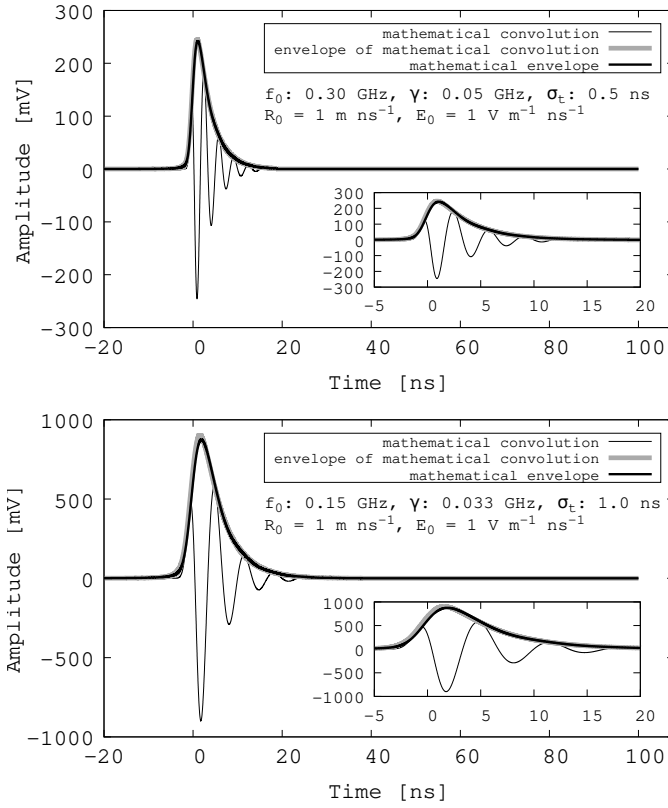
FIG. 1: (Top) The thin black line represents $s(t) * r(t)$. The light gray envelope represents the envelope of $s(t) * r(t)$ computed with the Python3 SciPy function scipy.special.hilbert. The dark gray envelope represents Eq. 51-53. (Bottom) Same as top, for different parameter values.

FIG. 2: (Top) The thin black line represents $s(t) * r(t)$, produced using the Python3 SciPy function scipy.signal.convolve. The dark gray line represents Eq. 61. (Bottom) Same as top, for different parameter values.

The detector was *a single string* of 8 RF dipoles, each with the same (x,y)-coordinates and regularly-spaced z-coordinates. The ice had a depth and radius of 0.65 km and 0.85 km, respectively, and the dielectric properties of the South Pole. Each RF channel had a filtered, amplified passband of [0.08-1] GHz, 256 samples, and a 1 GHz sampling rate. The RF trigger responded when any 3 of the 8 voltage traces exceeded ± 3 times the rms voltage ($v_{\rm rms}$) of the thermal noise (233K) within 256 ns. The Hilbert envelope of the coherently summed waveform (CSW) was calculated from the traces and cross-correlated with Eqs. 51-53. Each correlation was maximized by varying σ_t. An optimization using noiseless data (3K) yielded 0.15 GHz and 0.025 GHz for f_0 and γ, respectively. For each signal, a thermal noise trace satisfying the RF trigger was generated and cross-correlated against the best-fit analytic envelope. The results are shown in Fig. 3.

In Fig. 3, the circles represent the normalized histogram of the correlation coefficent between the optimized analytic envelope and thermal noise. A fitting function of the form $x^2 \exp(-0.5x^2)$ was fit to the noise distribution, and is represented by the gray dashed line. The solid gray line represents the signal distribution, which peaks at a correlation value of 0.94. Lower signal
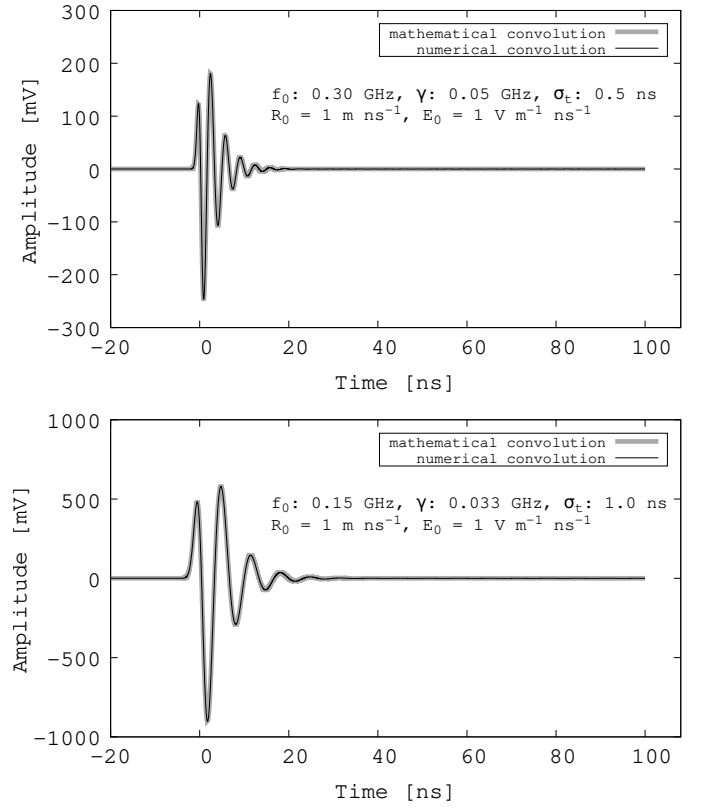
Parameter	Value	Note
Ice Model	South Pole	2015 measurements
Signal Model	ARZ2020	(see [13])
Trigger	3 of 8 channels	high-low trigger, $3v_{\rm rms}$
RF channels	8	RF bicone (in firn)
Channel filters	[80-1000] MHz	Passband
Noise Temperature	233K	Sets $v_{\rm rms}$
Sampling Rate	1 GHz	$f_c = 500$ MHz
Samples per channel	256	
Channel depths	[-4,-6,-8,...-18] m	cable delays included
RF cable type	LMR-400	< 0.0886 dB m^{-1}

TABLE II: Important NuRadioMC parameters used in this analysis.

correlation values correspond to lower SNR values (Fig. 4). The vertical black dashed line represents a threshold of 0.4. For the simulated UHE-ν, 99.99% of correlations exceed this threshold. Assuming a thermal trigger rate of 1 Hz, integrating the PDF of the noise distribution above the correlation threshold is equivalent to 0.2 noise events every 5 years. An example CSW fit by the analytic envelope is shown in Fig. 5.

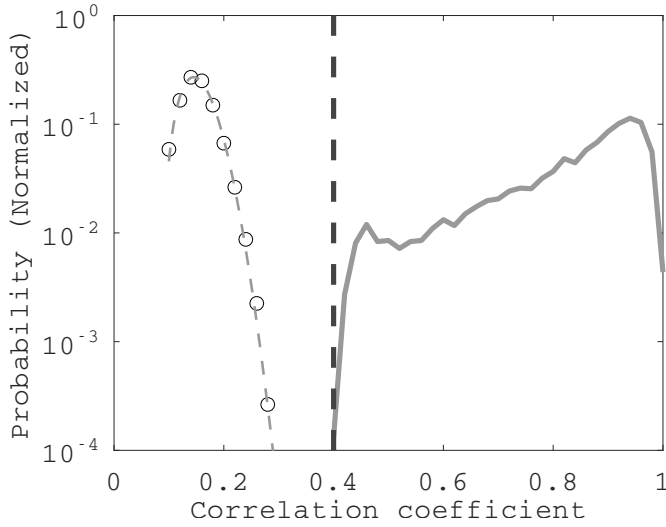The correlation between the optimized analytical en-

FIG. 3: (Black circles) Noise distribution. (Gray dashed line) Fitting function to noise distribution. (Solid gray line) UHE-ν signal distribution. (Dashed black line) Correlation threshold.
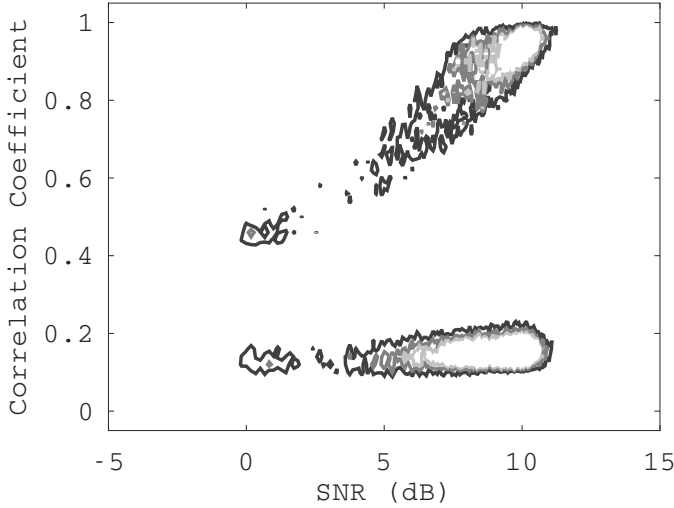

FIG. 4: The correlation versus SNR (dB) for UHE-ν signals (upper distribution) and RF thermal noise (lower distribution). Color scale: normalized histogram value, with five equally spaced contours between 0.0 and 0.002.

velope and UHE-ν signals depends on the signal to noise ratio (SNR). Let v_{pp} represent the peak-to-peak value in the voltage trace. The SNR (dB) is

$$\mathrm{SNR_{dB}} = 20 \log_{10} \left(\frac{1}{2} \frac{v_{\mathrm{pp}}}{v_{\mathrm{rms}}} \right) \qquad (62)$$

In Fig. 4, the correlation coefficient is plotted versus the SNR in dB for the data shown in Fig. 3. The upper and lower distributions correspond to CSWs from UHE-ν events and thermal noise, respectively. All RF thermal noise events satisfy the station trigger. Note that the cor-
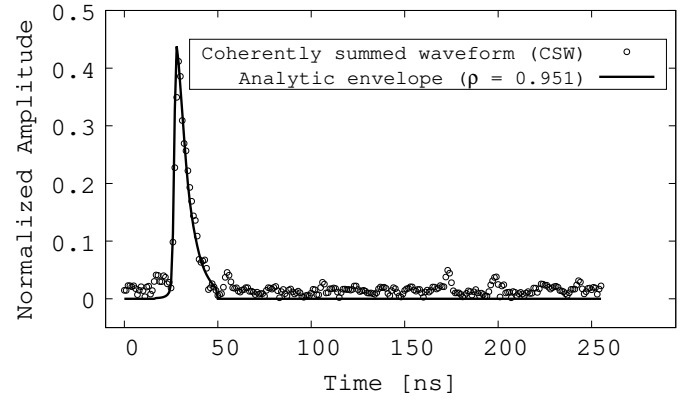

FIG. 5: A single-pulse CSW signal (black dots) from a 100 PeV UHE-ν, matched to an analytic envelope (thick black line) with a correlation coefficient $\rho = 0.951$.
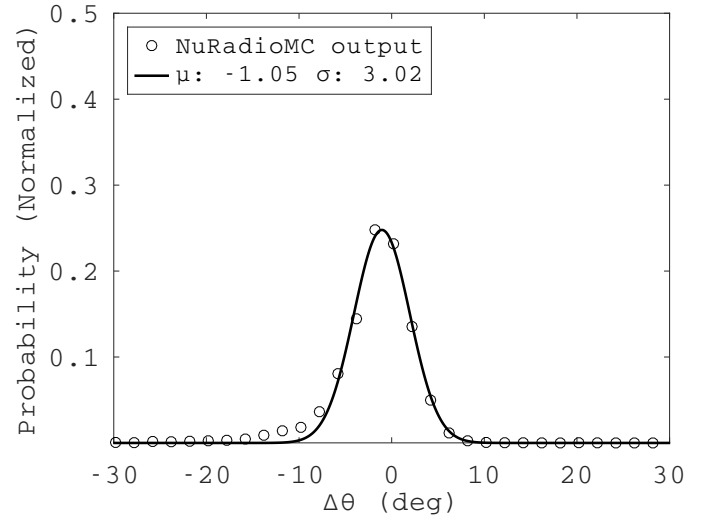

FIG. 6: (Black circles) Viewing angle from NuRadioMC. (Solid black line) Gaussian fit, with $\mu = -1.05$ deg, and $\sigma = 3.02$ deg. (Black dashed line) Cherenkov angle, θ_{C}.

relation coefficient for UHE-ν events is proportional to $\mathrm{SNR_{dB}}$. The SNR of a CSW does not equal the SNR of the individual voltage traces. Rather, the voltage traces will have SNRs 5-9 dB *lower* than the CSW. If N voltage traces contain signal, computing the CSW raises the linear SNR by a factor of $\sqrt{N}$, and adds $10 \log_{10}(N)$ to $\mathrm{SNR_{dB}}$. For an event with 3 of 8 channels containing signal, $10 \log_{10}(3) \approx 5$ dB, while $10 \log_{10}(8) \approx 9$ dB.

V. RECONSTRUCTION OF $\log_{10} E_{\mathrm{C}}$

Equations 5-8 may be used to reconstruct the natural logarithm of the UHE-ν cascade energy, $\ln \Lambda$. For Eq. 5, σ_t is measured from the optimized analytic envelope, c and θ_{C} are known constants. Without a separate fit for $\Delta \theta$ an assumption must be made. We will make the as-

sumption that $\Delta\theta \approx \Delta\theta_{\rm rms}$. The assumption is justified since the $\Delta\theta$ distribution is Gaussian. The MC truth for $\Delta\theta$ in this analysis is shown in Fig. 6, with a Gaussian fit. The rms and σ values are equal for normal distributions, so we let $\Delta\theta \approx \Delta\theta_{\rm rms}$ and set the fractional error $\sigma_{\Delta\theta}/\Delta\theta$ to 1.0. Solving Eq. 5 for a gives

$$a = \frac{c\sigma_t}{\Delta\theta_{\rm rms}\sin\theta_{\rm C}} \qquad (63)$$

The result for the fractional error in a is found by propagating error from σ_t and $\Delta\theta$, defined as ϵ and $\sigma_{\Delta\theta}$, respectively. The result is

$$\frac{\sigma_a}{a} = \left(\left(\frac{\epsilon}{\sigma_t}\right)^2 + \left(\frac{\sigma_{\Delta\theta}}{\Delta\theta}\right)^2 \right)^{1/2} \qquad (64)$$

The first term is small compared to the second, as it is limited by the scan resolution for σ_t and the number of samples per analytic envelope. The scan resolution is set to 0.2 ns in the optimization, and there are typically > 10 samples per envelope, or about 10 ns. Thus, $(\epsilon/\sigma_t)^2$ is two orders of magnitude smaller than $(\sigma_{\Delta\theta}/\Delta\theta)^2$, so

$$\frac{\sigma_a}{a} = \left| \frac{\sigma_{\Delta\theta}}{\Delta\theta} \right| = \left| \frac{\Delta\theta_{\rm rms}}{\Delta\theta_{\rm rms}} \right| \approx 1 \qquad (65)$$

Setting the ratio to 1 is a conservative assumption for $\ln\Lambda$, for inserting it into Eq. 8 gives

$$\frac{\sigma_{\ln\Lambda}}{\ln\Lambda} \approx 2 \qquad (66)$$

Using Eqs. 6 and 7, the logarithm of the energy is

$$\ln\Lambda = \left(\frac{c\sigma_t}{c_{\rm em/had}\Delta\theta_{\rm rms}\sin\theta_{\rm C}} \right)^2 \qquad (67)$$

Using Eqs. 10 and 12 from HH2022 ([11]), $c_{\rm em}$ and $c_{\rm had}$ were found to be 0.80 and 0.93 meters, respectively (FWHM, $R = 0.5$). Using Eq. 67, the σ_t results from the optimized envelope fits to UHE-ν signals may be used to deduce the logarithm of the UHE-ν cascade, $\log_{10} E_{\rm C}$. First, converting to the base-10 logarithm introduces a factor of $\ln(10)$ in the denominator of Eq. 67. Second, $\ln\Lambda = \ln(E_{\rm C}/E_{\rm crit})$, where $E_{\rm C}$ is the cascade energy, and $E_{\rm crit} \approx 10^8$ eV is known as the critical energy [11]. Since $\ln\Lambda = \ln E_{\rm C} - \ln E_{\rm crit}$, separating this ratio adds $\log_{10} E_{\rm crit}$ to the right hand side of Eq. 67. Third, let $c_{\rm ave}$ be the average of $c_{\rm em}$ and $c_{\rm had}$, reflecting the unknown hadronic or electromagnetic nature of the cascade. The modified form of Eq. 67 is

$$\log_{10} E_{\rm C} = \frac{(c\sigma_t)^2}{\ln 10 (c_{\rm ave}\Delta\theta_{\rm rms}\sin\theta_{\rm C})^2} + \log_{10} E_{\rm crit} \qquad (68)$$

Table III contains the results for the reconstruction of $\log_{10} E_{\rm C}$. The results are consistent with the MC truth. Note that when applying the change of base formula, factors of $\ln(10)$ cancel in the error ratio of Eq. 66, so the error in $\log_{10} E_{\rm C}$ remains 2.0. The σ_t result is the average value derived from 15133 UHE-ν events that triggered the detector with $E_{\rm C} = 100$ PeV. Note that the error in the *average* σ_t over all events fluctuates due to varying $\Delta\theta$, while the error in *individual* σ_t per CSW is small if the samples per CSW is much greater than 1. By far, the largest source of systematic error is *reflected signals*.

Multiple signals occur within traces either when signals from two ray-tracing paths are available, or when part of the signal reflects from the surface back to the channel. Signals that propagate directly to the detector are known as *direct signals*, while signals that reflect at the snow-air interface are known as *reflected signals*. Complex RF signal propagation in polar ice has been studied, and even proposed as a UHE-ν energy reconstruction technique [21, 24, 33]. When two signals are present in the voltage trace, the fitting algorithm favors σ_t values that are unphysically larger than the average quoted in Tab. III. This systematically overestimates $\log_{10} E_{\rm C}$. An example of a CSW event with direct and reflected components fit by an analytic envelope is shown in Fig. 7.

Parameter	Average Value
MC Truth, $E_{\rm C}$ [eV]	10^{17}
MC Truth, $\log_{10} E_{\rm C}$	17
c	0.3/1.78 m ns^{-1}
$\overline{\sigma_t}$	1.229 ± 0.004 ns
$c_{\rm ave}$	0.86 m
$\Delta\theta_{\rm rms}$	3.78 ± 0.04 degrees
$E_{\rm crit}$	100 MeV
$\sin\theta_{\rm C}$	0.8271
Reconstructed $\log_{10} E_{\rm C}$	16.5 ± 2.0

TABLE III: Energy reconstruction parameters used to calculate the logarithm of the UHE-ν cascade energy, $\log_{10} E_{\rm C}$.

VI. CONCLUSION

In Secs. I and refsec:unit, previous work in the utility of analytic Askaryan models was reviewed, and important parameters were defined. In Sec. III, a fully analytic model for $\mathcal{E}_{\rm s*r}(t)$ and $s(t) * r(t)$ was presented and checked for accuracy. In Sec. IV, the analytic model was shown to reject all but 0.2 RF thermal triggers in a 5 year run at a 1 Hz thermal trigger rate using a correlation threshold of 0.4. That same threshold preserves 99.99% of UHE-ν signals at 100 PeV. The correlation distribution for UHE-ν signals peaked at 0.94, and some values even exceed 0.94. Finally, in Sec. V, a first attempt at using the CSW fit with data *a single-string detector* to reconstruct $\log_{10} E_{\rm C}$ was presented. Though the error
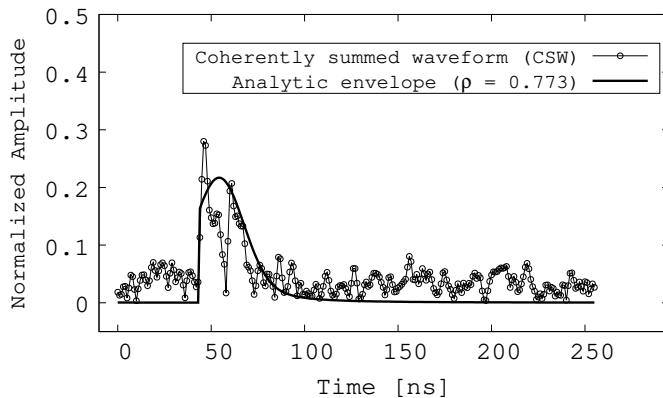
FIG. 7: A CSW signal with a reflection (black dots and thin black line) from a 100 PeV UHE-ν, matched to an analytic envelope (thick black line), with $\rho = 0.773$.

range for $\log_{10} E_C$ is large, the average value is correct: $\log_{10} E_C = 16.5 \pm 2.0$ for 100 PeV.

There are three logical steps for this work in the future. First, we must account for multiple pulses in the algorithm used to fit the analytic envelope to CSWs from NuRadioMC. The authors of [33] have shown how direct and reflected (DnR) signals may be used to constrain the UHE-ν energy. This procedure should be combined with

the analytic envelope fit to advance UHE-ν energy reconstruction. Though this is not difficult to implement in NuRadioMC, it was beyond the scope of this work.

Second, we should be able to incorporate a separate fit for $\Delta\theta$. This parameter may be constrained by using the spectral cutoff, which is inversely correlated to $\Delta\theta$ [12]. With a separate fit for $\Delta\theta$, the a-value could be constrained without making any assumption about $\Delta\theta$. This step would improve the precision of the a-value by lowering the fractional error in a-values in Eq. 64.

Third, it is interesting to note that the entire model relies on the *off-cone* ($\theta \neq \theta_C$) version of $s(t)$. HH2022 also includes an *on-cone* version of $s(t)$ that is used when $\Delta\theta \lesssim 1$ degree. The on-cone model could provide a better fit between $\mathcal{E}_{s*r}(t)$ for events with $\Delta\theta \lesssim 1$ degree.

[1] The IceCube Collaboration, Science **342**, 1242856 (2013), ISSN 0036-8075, 1311.5238.

[2] The IceCube Collaboration, Physical Review Letters **111**, 021103 (2013), ISSN 0031-9007, 1304.5356.

[3] The IceCube Collaboration, The Astrophysical Journal **833**, 3 (2016), ISSN 0004-637X, 1607.08006.

[4] The IceCube Collaboration, Science **361**, 147 (2018), ISSN 0036-8075, 1807.08794.

[5] The IceCube Collaboration, Nature **591**, 220 (2021), ISSN 0028-0836, 2110.15051.

[6] The IceCube Collaboration, Science **378**, 538 (2022), ISSN 0036-8075.

[7] The IceCube Collaboration, Science **380**, 1338 (2023), ISSN 0036-8075.

[8] The KM3NeT Collaboration, Nature **638**, 376 (2025), ISSN 0028-0836.

[9] The IceCube Collaboration, Physical Review D **98**, 062003 (2018), ISSN 2470-0010, 1807.01820.

[10] The IceCube-Gen2 Collaboration, arXiv (2020), 2008.04323.

[11] J. C. Hanson and R. Hartig, Phys. Rev. D **105**, 123019 (2022), URL https://link.aps.org/doi/10.1103/PhysRevD.105.123019.

[12] J. C. Hanson and A. L. Connolly, Astroparticle Physics **91**, 75 (2017), ISSN 0927-6505.

[13] J. Alvarez-Muniz, P. M. Hansen, A. Romero-Wolf, and E. Zas, Phys. Rev. D **101**, 083005 (2020), URL https://link.aps.org/doi/10.1103/PhysRevD.101.083005.

[14] J. C. Hanson et al, Astroparticle Physics **62**, 139 (2015), ISSN 0927-6505, 1406.0820.

[15] J. C. Hanson et al, Journal of Glaciology **61**, 438 (2015), ISSN 0022-1430.

[16] J. Avva, J. Kovac, C. Miki, D. Saltzberg, and A. Vieregg, Journal of Glaciology (2014), 1409.5413.

[17] D. Saltzberg, P. Gorham, D. Walz, C. Field, R. Iverson, A. Odian, G. Resch, P. Schoessow, and D. Williams, Physical review letters **86**, 2802 (2001), ISSN 0031-9007.

[18] P. Miocinovic, R. Field, P. Gorham, E. Guillian, R. Milincic, D. Saltzberg, D. Walz, and D. Williams, Physical Review D **74**, 043002 (2006), ISSN 2470-0029, hep-ex/0602043.

[19] P. W. Gorham, S. W. Barwick, J. J. Beatty, D. Z. Besson, W. R. Binns, C. Chen, P. Chen, J. M. Clem, A. Connolly, P. F. Dowkontt, et al. (ANITA Collaboration), Phys. Rev. Lett. **99**, 171101 (2007), URL https://link.aps.org/doi/10.1103/PhysRevLett.99.171101.

[20] C. Glaser et al, The European Physical Journal C **80**, 77 (2020), ISSN 1434-6044, 1906.01670.

[21] The ARIANNA Collaboration, Journal of Cosmology and Astroparticle Physics **2018** (2018).

[22] The ARA Collaboration, Astroparticle Physics **108**, 63 (2019), ISSN 0927-6505, URL https://www.sciencedirect.com/science/article/pii/S0927650518301154.

[23] The ARIANNA Collaboration, Journal of Instrumentation **15**, P09039 (2020), 2006.03027.

[24] C. Deaconu, A. G. Vieregg, S. A. Wissel, J. Bowen, S. Chipman, A. Gupta, C. Miki, R. J. Nichol, and D. Saltzberg, Physical Review D **98**, 043010 (2018), ISSN 2470-0010, 1805.12576.

[25] C. Welling and T. R.-G. Collaboration, The Cryosphere **18**, 3433 (2024).

[26] R. V. Buniy and J. P. Ralston, Physical Review D **65** (2001), ISSN 2470-0029.

[27] E. Zas, F. Halzen, and T. Stanev, Physical Review D **45**, 362 (1992).

[28] DLMF, *NIST Digital Library of Mathematical Functions*, http://dlmf.nist.gov/, Release 1.1.1 of 2021-03-15, f. W. J. Olver, A. B. Olde Daalhuis, D. W. Lozier, B. I. Schneider, R. F. Boisvert, C. W. Clark, B. R. Miller, B. V. Saunders, H. S. Cohl, and M. A. McClain, eds., URL `http://dlmf.nist.gov/`.

[29] G. B. Rybicki, Computers in Physics **3**, 85 (1989), ISSN 0894-1866.

[30] J. A. Aguilar, P. Allison, J. J. Beatty, H. Bernhoff, D. Besson, N. Bingefors, O. Botner, S. Buitink, K. Carter, B. A. Clark, et al., Journal of Instrumentation **16**, P03025 (2021), 2010.12279.

[31] I. Kravchenko et al, Physical Review D **85**, 062004 (2012), ISSN 2470-0029, 1106.1164.

[32] J. Alvarez-Muniz, A. Romero-Wolf, and E. Zas, Physical Review D **84**, 103003 (2011), ISSN 2470-0029, 1106.6283.

[33] A. Anker, S. Barwick, H. Bernhoff, D. Besson, N. Bingefors, D. García-Fernández, G. Gaswint, C. Glaser, A. Hallgren, J. Hanson, et al., Journal of Cosmology and Astroparticle Physics **2019**, 030 (2019), 1909.02677.